Manuscript prepared for Atmos. Chem. Phys.
with version 2015/04/24 7.83 Copernicus papers of the LaTeX class copernicus.cls.
Date: 10 December 2015

The tropopause inversion layer in baroclinic life cycle experiments: the role of diabatic processes

Daniel Kunkel[1], Peter Hoor[1], and Volkmar Wirth[1]

[1]Institute for Atmospheric Physics, Johannes-Gutenberg University Mainz, Germany

Correspondence to: Daniel Kunkel (dkunkel@uni-mainz.de)

Abstract. Recent studies on the formation of a quasi-permanent layer of enhanced static stability above the thermal tropopause revealed the contributions of dynamical and radiative processes. Dry dynamics lead to the evolution of a tropopause inversion layer (TIL) which is, however, too weak compared to observations and thus diabatic contributions are required. In this study we aim to assess the importance of diabatic processes in the understanding of TIL formation at midlatitudes. The non-hydrostatic model COSMO is applied in an idealized mid-latitude channel configuration to simulate baroclinic life cycles. The effect of individual diabatic processes related to humidity, radiation, and turbulence is studied first to estimate the contribution of each of these processes to the TIL formation in addition to dry dynamics. In a second step these processes are stepwise included in the model to increase the complexity and finally estimate the relative importance of each process. The results suggest that including turbulence leads to a weaker TIL than in a dry reference simulation. In contrast, the TIL evolves stronger when radiation is included but the temporal evolution is still comparable to the reference. Using various cloud schemes in the model shows that latent heat release and consecutive increased vertical motions foster an earlier and stronger appearance of the TIL than in all other life cycles. Furthermore, updrafts moisten the upper troposphere and as such increase the radiative effect from water vapor. Particularly, this process becomes more relevant for maintaining the TIL during later stages of the life cycles. Increased convergence of the vertical wind induced by updrafts and by propagating inertia-gravity waves, which potentially dissipate, further contributes to the enhanced stability of the lower stratosphere. Furthermore, radiative feedback of ice clouds reaching up to the tropopause is identified to potentially further affect the strength of the TIL in the region of the clouds.

1 Introduction

The sharpness of the tropopause in the extratropics has gained increased attention in recent years (e.g., Gettelman and Wang, 2015). Local maxima of static stability, usually measured by the squared Brunt–Vaisala frequency $N^2 = g/\Theta \cdot \partial\Theta/\partial z$ with g, the gravitational acceleration, Θ, the potential temperature, and z, the geometric altitude, inferred from radiosonde measurements (e.g., Birner

et al., 2002; Birner, 2006) and Global Positioning System (GPS) radio occultation measurements (Randel et al., 2007), revealed the existence of a quasi-permanent inversion layer above the thermal tropopause. This tropopause inversion layer (TIL) is a distinct feature of the region of the upper troposphere and lower stratosphere (UTLS), from tropical to polar regions (e.g., Grise et al., 2010) and is also evident in general circulation models and climate analysis data sets (e.g., Birner et al., 2006).

Global studies of GPS temperature profiles and reanalysis data sets showed that the TIL is present at all latitudes (Grise et al., 2010; Gettelman and Wang, 2015). In the tropical lower stratosphere two maxima of enhanced static stability are found at about 17 and 19 km altitude. The upper peak shows a seasonal cycle with a winter maximum, while the lower peak has relatively large values all year round (Grise et al., 2010). In polar regions a distinct summer maximum occurs (Randel and Wu, 2010), while the TIL is evident in midlatitudes throughout the entire year with a slightly deeper appearance during winter (Bell and Geller, 2008). Generally, the smallest values of static stability above the thermal tropopause are evident in the region of the subtropical jet (Grise et al., 2010).

In several studies it was shown that a TIL can form from balanced, adiabatic and frictionless dynamics without explicit contributions from radiation in the extratropics. These idealized model simulations span the range from local to global scales, with studies of the dynamics of upper-level anomalies of potential vorticity (further abbreviated with PV) (Wirth, 2003, 2004), of baroclinic life cycles (Erler and Wirth, 2011), and of the dynamical response to a forcing of a Held–Suarez test (Held and Suarez, 1994) in a dry general circulation model (Son and Polvani, 2007). In the latter case, the TIL forms spontaneously under a wide variety of model parameters, such as horizontal and vertical model resolution. From the analysis of positive and negative PV-anomalies it was found that the sharpening of the tropopause was linked to the convergence of the vertical wind. Particularly, this was related to a cross-frontal circulation (Wirth, 2004). Furthermore, the TIL evolved stronger above anti-cyclonic than over cyclonic flow (Wirth, 2003). This result was confirmed in studies of adiabatic baroclinic life cycles, in which the TIL became evident after breaking of baroclinic waves (Erler and Wirth, 2011). Recently, the impact of dissipating inertia-gravity waves was suggested to persistently contribute to the formation and maintenance of the TIL. These waves result from imbalances along the jet and the dissipation may alter the thermal structure through energy dissipation, local heating, and turbulent motions (Kunkel et al., 2014). Moreover, Birner (2010) showed that the vertical structure of the residual circulation in the stratosphere contributes to the sharpening of the tropopause by inducing a dipole forcing of static stability around the tropopause. This process was identified to significantly add to the tropopause sharpening during winter in the midlatitudes.

Balanced dynamics alone, however, can not explain all features related to the TIL (Son and Polvani, 2007) and as has been shown by Randel et al. (2007) radiative processes contribute significantly to the TIL. From fixed dynamical radiative transfer calculations it was concluded that water vapor cooling around the tropopause and heating by ozone in the lower and middle strato-

sphere contribute to a layer of enhanced static stability above the thermal tropopause. Particularly, the water vapor cooling has been identified to be a major process for the summer TIL in polar regions (Randel and Wu, 2010).

Thus, several mechanisms have been identified so far to explain the strength and occurrence of the TIL at all latitudes. Since dry dynamics are not sufficient to fully explain all features of the TIL, processes beyond adiabatic and frictionless dynamics are required to close this gap. Especially in the midlatitude tropopause region, all processes, synoptic-scale and stratospheric dynamics as well as the radiative forcings, need to be considered. With this knowledge we can ask the question which of the before mentioned processes is most important to form and maintain the TIL. In this study we aim to address this question in the framework of idealized baroclinic life cycles with a limited area, non-hydrostatic model. We extend the work of Erler and Wirth (2011) and include diabatic processes, i.e., related to humidity, radiation, or turbulence. These processes can violate material conservation of potential vorticity Q and are further referred to as non-conservative processes in this study. Since we focus on a rather short time scale, we assume that the effect of the stratospheric circulation is rather small and exclude this effect in the interpretation of our results. Thus, we focus mainly on the following questions: (1) How do non-conservative processes, i.e., diabatic processes, alter the TIL evolution in baroclinic life cycles compared to the well-known evolution in the adiabatic and frictionless case? (2) What is the relative importance of individual processes that contribute to the formation the TIL during different stages of the life cycles?

To answer these questions we structured our analysis as follows. In Sect. 2 we introduce the model setup along with the physical parameterizations and a summary of the conducted simulations. We then present results from two sets of simulations of so-called anti-cyclonic life cycles. In Sect. 3 we show results from baroclinic life cycles in which only one individual non-conservative process is turned on separately to address question (1). In a second set of simulations we show results of simulations with a successively increasing number of physical processes to address question (2) (Sect. 4). Before we summarize our results and give further conclusions in Sect. 6, we discuss the evolution of the tropopause inversion layer in experiments of the cyclonic life cycle in Sect. 5.

2 Model formulation and baroclinic life cycle experiments

2.1 Adiabatic model configuration and initial state

We conducted baroclinic life cycle experiments in an idealized, spherical, midlatitude channel configuration of the non-hydrostatic regional model COSMO (COnsortium for Small-scale MOdelling, Steppeler et al., 2003). For the adiabatic model we only use the dynamical core of the model which solves the hydro-thermodynamical equations. Only a fourth order horizontal hyper-diffusion has to be applied to guarantee numerical stability. Physical processes such as microphysics, convection, turbulence, radiation are introduced in more detail further below (see Sect. 2.2). Time integration is

performed with a third order, two-time-level Runge–Kutta scheme, in which fast terms, i.e., sound and gravity waves, are stepped forward in time with a smaller time step. We use a fifth order centered finite difference approximation in the horizontal and a third order scheme in the vertical. Passive tracer advection is done with a fourth order Bott Scheme with Strang splitting (Doms, 2011).

We study baroclinic waves with wavenumber six with a model setup similar to Erler and Wirth (2011) and Kunkel et al. (2014). Our model domain spans over 60° longitude and 70° latitude, from the surface up to a height of $25.0\,\mathrm{km}$ and with a grid spacing of 0.4° ($\sim 44\,\mathrm{km}$) in the horizontal and $110\,\mathrm{m}$ in the vertical in the region of the tropopause. Consequently, we obtain an aspect ratio ($\Delta z/\Delta x$) of about $1/400$ which is considered favorable to study the TIL (Birner et al., 2006; Erler and Wirth, 2011). In the uppermost seven kilometer of the model domain Rayleigh damping is applied to avoid reflection of upward propagating signals and there is no orography at the bottom. In meridional direction the boundary conditions are relaxed towards the initial values to avoid reflection of outgoing signals, while periodic boundary conditions are specified in the zonal direction.

For the initial conditions we follow Olson and Colle (2007) and Schemm et al. (2013) with slight adaptations to account for the spherical geometry of our approach. A background state is obtained for three dimensional fields of temperature, T, and pressure, p, from which a thermally balanced wind is calculated as in Erler and Wirth (2011). The initial vertical wind, w, is zero and the background state is baroclinically unstable by construction. However, to allow a fast evolution of the baroclinic wave, this state is superimposed by perturbation fields for p, T, u, and v which result from an inversion of a specified PV anomaly. This circular anomaly is introduced in the middle of the domain at the altitude of the tropopause. Slight changes in the initial state allow us to study various types of baroclinic life cycles (for details we refer to Olson and Colle, 2007). To obtain a solution of our experiments that is known as LC2 (Thorncroft et al., 1993), an additional cyclonic barotropic shear is added to the background state described above. However, the main focus of this study is on the classical LC1 wave type (Thorncroft et al., 1993), since it produces a stronger TIL in the adiabatic case (Erler and Wirth, 2011). In Section 5 we will present differences in the evolution of the TIL in LC2 experiments. The LC1 type is characterized by a thinning trough which then forms a streamer and later a cut-off cyclone, while the baroclinic wave breaks anti-cyclonically. Thus, the LC1 is also known as the anti-cyclonic case. In contrast, in the LC2 a large cyclonic trough dominates the evolution of the wave with no streamer and no cut-off cyclone being evident. This case is known as the cyclonic case, since the wave breaks cyclonically. More details on the development of these waves and the corresponding evolution of the tropopause inversion layer are generally given in Erler and Wirth (2011) and for the LC1 setup specifically in Kunkel et al. (2014), where the authors used a higher resolution version of this model. It is noted here that the lower resolution model well reproduces the results of Kunkel et al. (2014). For this reason and because of the vast number of conducted model simulations (see Table 1), we decided to use a coarser grid spacing in our simulations.

Figure 1 shows the initial state in the center of our model domain. The zonal wind u has its maximum velocity between the thermal and dynamical tropopause (here defined as the $Q = 2.0\,\mathrm{pvu}$ contour line, with pvu = potential vorticity units, and $1.0\,\mathrm{pvu} = 1.0 \times 10^{-6}\,\mathrm{K\,m^2\,kg^{-1}\,s^{-1}}$). For the thermal tropopause we follow the definition given in *WMO* (1957), where the tropopause is defined as the lowest level where the temperature lapse rate falls below $2.0\,\mathrm{K\,km^{-1}}$ and its average between this level and all higher levels within two km above this level remains below this value. The thermal tropopause further separates tropospheric ($N^2 < 1.5 \times 10^{-4}\,\mathrm{s^{-2}}$) from the stratospheric ($N^2 > 4.0 \times 10^{-4}\,\mathrm{s^{-2}}$) background values of static stability. The initial zonally symmetric specific humidity field, depicted with the blue lines, has been constructed such that it is comparable in magnitude and distribution to moisture profiles from re-analysis data. For this it is constructed as follows: a constant surface relative humidity ($\mathrm{RH_s}$) is given which decreases linearly with height everywhere. If not specified otherwise, $\mathrm{RH_s}$ is $60\,\%$ and decreases with a gradient of $10\,\%/2\,\mathrm{km}$. Thus, above $12\,\mathrm{km}$ altitude the relative humidity (RH) is zero. The model, however, requires specific humidity q_v as input variable. This quantity is obtained by multiplication of the relative humidity with the saturation specific humidity ($q_\mathrm{vs} : q_\mathrm{v} = \mathrm{RH}/100 \cdot q_\mathrm{vs}$). The latter quantity is computed from the saturation water vapor, which is computed with the parameterization of Magnus (Murray, 1967). A final constraint is given for the initial distribution of q_v, i.e., that $\min(q_\mathrm{v}) = 2.0 \times 10^{-6}\,\mathrm{kg\,kg^{-1}}$. Note that this leads to a constant initial value of $q_\mathrm{v} = 2.0 \times 10^{-6}\,\mathrm{kg\,kg^{-1}}$ in the stratosphere in our simulations.

We further use passive tracers to diagnose particular features of our baroclinic life cycles. These tracers are purely advected and not explicitly mixed vertically or horizontally by a parameterization scheme. However, mixing due to numerical reasons does still affect the tracer distribution. In particular, we use three tracers which carry information of the initial state of the baroclinic life cycles: (1) the initial height of each grid box z_0, (2) the initial static stability N_0^2, and (3) the initial potential vorticity Q_0. With these tracers it is possible to calculate the differences between the current and the initial distribution of these quantities and as such obtain information about whether an air parcel has gained or lost (1) altitude, measured by $\Delta z = z - z_0$, (2) static stability, measured by $\Delta N^2 = N^2 - N_0^2$, and (3) changed their potential vorticity because of non-conservative processes, measured by $\Delta Q = Q - Q_0$, with $Q = \varrho^{-1}\boldsymbol{\eta} \cdot \nabla\Theta$ and ϱ air density, $\boldsymbol{\eta}$ absolute vorticity, and Θ potential temperature. We want to note here that we will use positive values of Δz as a predictor of vertically ascending air masses. In this study we will also use the term updraft to describe these air masses, independently of the cause of the ascent, e.g., frontal or convective, and of any time period in which the ascent has occurred. The only criteria are that Δz is larger than $2.5\,\mathrm{km}$ and that these air masses reach the altitude of the tropopause.

2.2 Formulation of non-conservative processes in COSMO

2.2.1 Turbulence

Turbulence is calculated for the three dimensional wind (u, v, and w), the liquid water potential temperature (Θ_l), and the total water (q_w) which is the sum of specific water vapor q_v and specific cloud water q_c. Budget equations for the second order moments are reduced under application of a closure of level 2.5 (in the notation of Mellor and Yamada, 1982), i.e., local equilibrium is assumed for all moments except for turbulent kinetic energy (TKE), for which advection and turbulent transport is retained. Three dimensional turbulent effects are neglected which is a valid approximation for simulations on the mesoscale, which means that horizontal homogeneity is assumed. Hence, only vertical turbulent fluxes are parameterized under consideration of the Boussinesq approximation. Moreover, the TKE budget equation depends significantly on the vertical shear of the horizontal wind components and the vertical change in Θ_l and q_w. More details are given in Doms (2011).

2.2.2 Cloud microphysics

Cloud microphysics follow a bulk approach using a single moment scheme with five types of water categories being treated prognostically: specific humidity q_v for the gas phase, two non-precipitating cloud types, i.e., cloud water q_c and cloud ice q_i, as well as two precipitating types, i.e., rain q_r and snow q_s. These five water types can interact within various processes such as cloud condensation and evaporation, depositional growth and sublimation of snow, evaporation of snow and rain, melting of snow and cloud ice, homogeneous and heterogeneous nucleation of cloud ice, autoconversion, collection and freezing. More details are given in Doms (2011) and Joos and Wernli (2012).

2.2.3 Radiation

Radiation is parameterized by the δ-2 stream approximation, i.e., separate treatment of solar and terrestrial wavelengths. In total, eight spectral bands are considered, five in the solar range and three infrared bands. Absorbing and scattering gases are water vapor ($\mathrm{H_2O}$) with a variable content as well as $\mathrm{CO_2}$, $\mathrm{O_3}$, $\mathrm{CH_4}$, $\mathrm{N_2O}$, and $\mathrm{O_2}$ with fixed amounts. Aerosols have been totally neglected whereas a cloud radiative feedback can be calculated in all spectral bands. Further details about the general scheme are given in Ritter and Geleyn (1992) and about the implementation in Doms (2011).

2.2.4 Convection

The scheme of Tiedtke (1989) is used to parameterize sub-grid scale convective clouds and their effects on the large scale environment. This approach uses moisture convergence in the boundary layer to estimate the cloud base mass-flux. The convection scheme then affects the large-scale budgets of the environmental dry static energy, the specific humidity, and the potential energy.

2.2.5 Surface fluxes

Instead of using a bottom free-slip boundary condition surface fluxes of momentum and heat are calculated explicitly in one experiment. This results in non-zero turbulent transfer coefficients of momentum and heat and thus affects the roughness length and the fluxes of latent and sensible heat. As we will show later, this has some significant effects on the initiation of convection.

2.3 Simulations of baroclinic life cycles

In total we present the results of 17 different simulations of the anti-cyclonic and of five different simulations of the cyclonic baroclinic life cycle (see Table 1). Variations between the individual simulations are introduced by either the kind or the number of non-conservative processes. Moreover, additional variability is created by changing the initial humidity as well as by the complexity of treating cloud related processes.

In a first set of simulations, we conducted four different baroclinic life cycles. Using the adiabatic and frictionless life cycle as conservative reference simulation (REF), we obtain further results from life cycles additionally including either turbulence, further denoted as TURB, or radiation, RAD, or bulk microphysics, BMP. For these simulations we apply the standard physical parameterizations of COSMO, which were briefly described in the previous section.

We performed further sensitivity simulations for BMP and RAD to test for the impact of initial conditions as well as the model formulation of a diabatic process. For microphysics we conducted in total four additional life cycle experiments. We first tested for the initial specific humidity q_v. In one case we reduced the initial q_v by setting the surface relative humidity to $30\,\%$ and the gradient to $5.0\,\%/2\,\mathrm{km}$ (BMP R30), while we increased the initial q_v by using $\mathrm{RH_s} = 80\,\%$ and a gradient of $13.33\,\%/2\,\mathrm{km}$ in another case (BMP R80). Furthermore, we conducted simulations in which we used different schemes to represent cloud processes. In one simulation only warm phase clouds are considered, excluding cloud ice (BMP NOICE). In another simulation condensation and evaporation between water vapor and cloud water is realized by a saturation adjustment process (BMP SATAD). Since this simulation includes only large scale diabatic effects from latent heating, it has the least additional effects compared to the dry reference (Schemm et al., 2013).

In case of radiation we performed sensitivity simulations with respect to the initial distribution of specific humidity and ozone. These two trace gases are thought to have the largest impact on the thermal structure around the tropopause (e.g., Randel et al., 2007; Riese et al., 2012). We conducted one simulation with reduced initial specific humidity (RAD R30), similar to BMP R30, while we explicitly set the specific humidity to zero above the tropopause in another simulation (RAD woSW). In another case we reduced the amount of ozone (RAD rO3). However, we explicitly note here that ozone is poorly represented in the model. Instead of a three dimensional distribution, only a simple vertical distribution is assumed which has a maximum concentration at altitudes which are close

to our model top at a pressure of $42\,\mathrm{hPa}$ and a total vertically integrated ozone partial pressure of $0.06\,\mathrm{Pa}$. These two parameters are used in the radiation code to calculate the feedback of the solar and thermal extinction by ozone. We reduced the total amount of ozone by one third to estimate whether this has an impact on the strength of the TIL.

In a next step we use a set of simulations with combinations of non-conservative processes to study potential additive effects as well as to assess the relative contribution of individual processes on the TIL formation and maintenance during different stages of the life cycles. For this we compare results from BMP (here as a reference) to results from simulations where we first add radiation (BMP RAD) and turbulence (BMP TURB) individually and then together (abbreviated with BRT for BMP RAD TURB). In further simulations we include convective clouds (BRTC) and surface fluxes (BRTCS). The convective activity is much stronger in the simulation with surface fluxes than in the simulation with the free-slip boundary condition. Hence, BRTCS can be regarded as simulation with strong convection, while BRTC can rather be seen as life cycle with weak to moderate convective activity. A final sensitivity study was conducted in which the cloud radiative forcing has been neglected to study the effect of this feedback in the region of the tropopause (BMP RAD NOCRF).

3 Non-conservative processes and the formation of a TIL in baroclinic life cycles

In a first step we aim to answer the question which non-conservative process, i.e., related to clouds, radiation, or turbulent mixing has the largest impact on the formation of the TIL in baroclinic life cycles. For this we compare first the results of four anti-cyclonic life cycles (REF, TURB, RAD, and BMP), before we discuss the effects of initial conditions and process formulations on the model results.

3.1 Impact of non-conservative processes on the TIL evolution

The baroclinic life cycle 1, also known as LC1, has been discussed under various aspects (e.g., Thorncroft et al., 1993) and also in light of the evolution of the tropopause inversion layer (Erler and Wirth, 2011). Our REF simulation features the same general characteristics of this life cycle and is described in more detail in Kunkel et al. (2014). One dominant feature of the LC1 is the thinning trough, the so-called stratospheric streamer (often also referred to as Θ- or PV-streamer, e.g., Sprenger et al., 2003). In the mature stage of the baroclinic wave this feature is evident for instance in the distribution of potential temperature Θ on an isosurface of potential vorticity, e.g., $Q = 2.0\,\mathrm{pvu}$. The distribution of potential temperature for our four cases is shown in the upper row of Fig. 2. After $120\,\mathrm{h}$ of model integration we see similar structures for REF, TURB, and RAD with minor differences in the exact location of the streamer and the absolute values of Θ in the warm sector (red colors). The most complex distribution occurs in BMP with warmer temperatures than

in the other three simulations at the southern tip of the streamer. These warmer temperatures are associated with cloud processes and the release of latent heat during rapid ascent. Moreover, the entire Θ-field shows a more in-homogeneous appearance compared to the other three simulations.

Our main focus is, however, on the static stability N^2 in the lowermost stratosphere. In particular, we are interested in the regions where the stability increases significantly during the life cycle. This is typically the case within the first kilometer above the thermal tropopause. However, the spatial appearance is not homogeneous, as is evident from the lower panels in Fig. 2. These panels depict the vertical mean of N^2 over the first kilometer above the thermal tropopause. In all four cases large values of N^2 appear in the warm sector west of the streamer, which is in the region of anti-cyclonic flow. This region has been shown to exhibit a stronger TIL in models (Erler and Wirth, 2011; Wirth, 2003) and in observations (Randel et al., 2007). The life cycle with turbulence shows the lowest values of N^2, while the static stability has generally larger values in the case of radiation than in the reference simulation. In the life cycle with cloud processes we additionally see enhanced values of N^2 on smaller scales than in the other cases. As we will show later these enhancements are related to moist dynamics and vertical motions.

The moist life cycle shows the strongest development in terms of minimum surface pressure, p_s, evolution, in contrast to the life cycle with radiation (Fig. 3a). While all other life cycles show still a deepening of p_s, the absolute minimum pressure has already been reached in BMP after $140\,\mathrm{h}$ of model integration. Moreover, by considering two metrics to trace the evolution of the TIL in our life cycles, we infer that the TIL formation differs most significantly from the dry reference case in the moist life cycle. The maximum static stability N^2_max increases rather suddenly in BMP instead of more gradually as in the other three simulations (Fig. 3b). After reaching its absolute maximum value, N^2_max keeps values above $7.0 \times 10^{-4}\,\mathrm{s}^{-2}$ at consecutive times. Only after about $130\,\mathrm{h}$ after model start N^2_max in RAD, and a little bit later in REF and TURB, has reached the same magnitude as in the moist simulation. Furthermore, an earlier increase of N^2_max is evident in RAD than in REF and TURB, while in the latter case N^2_max is smaller than in the reference case at all times. A similar picture is obtained from the metric that is used as a proxy for the spatial extent of the TIL in the life cycles, i.e., the area in which $N^2 > 5.5 \times 10^{-4}\,\mathrm{s}^{-2}$, denoted as $A_{5.5}$ (Fig. 3c). The earliest appearance is evident in BMP, the latest in TURB. Moreover, the temporal evolution of $A_{5.5}$ clearly shows that the TIL covers a larger area when moist or radiative processes are included in the life cycles. We also tested other thresholds for N^2 for this metric with no significant changes with respect to the qualitative interpretation of our results.

So far, we provided a rather descriptive view on the TIL evolution in our life cycles without giving details about the underlying processes. For the case with turbulence the TIL appears weaker due to the tendency of turbulence to reduce strong vertical gradients. Turbulence acts against the effects of dry dynamics which enhance the lower stratospheric stability during the life cycle. Consequently, only a weak TIL forms in this case.

Including radiation results in a stronger TIL than in the reference case. This is related to the radiative feedback of water vapor, which increases over time in the region of the tropopause (Fig. 4a). Since no microphysics is included in RAD, water vapor is transported as a passive tracer in this simulation. Upward motions in the troposphere and tropopause dynamics lead to more water vapor at the altitude of the tropopause, finally changing the water vapor gradient significantly (Fig. 4b). This causes differential cooling by water vapor in the UTLS, which then results in a non-uniform change of the thermal structure (e.g., Zierl and Wirth, 1997). Additionally, recently lifted, moist air is then partly located also in the lower stratosphere, where its residence time is longer and thus can potentially affect the thermal structure over longer time scales. This process further enhances the static stability directly above the tropopause and thus strengthens the TIL which also forms by the dynamics of the baroclinic wave. Thus, a process directly changing the thermal structure alters the appearance of the TIL in the case with radiation.

In the moist case we present evidence that a process at lower tropospheric levels is responsible for the different appearance of the TIL. The spontaneous increase in N^2_{max} is well correlated with the earliest release of latent heat in the model (Fig. 5a and b). Since the same effect is evident from the simulation with the saturation adjustment scheme (BMP SATAD), we can conclude that it is the release of latent heat rather than a microphysical process being responsible for the observed effect. Latent heat release is, however, not only a sign of condensation but also fosters vertical motions in the model. These vertical motions reach in many cases the tropopause and often lift this vertical transport barrier. Consequently, also the air above is slightly lifted, thereby increasing the vertical gradient of potential temperature, resulting in enhanced static stability above the tropopause. This process differs, however, fundamentally from the process related to dry dynamics on spatial and temporal scales. While the latter is rather slow and occurs predominantly in an anti-cyclonic flow region with on average descending air motion, this lifting process is fast, occurs on small scales, and is related to upward motions. Thus taken together, the incorporation of water in the model fosters a stronger TIL development as consequence of enhanced upward motions within the life cycle due to the release of latent heat.Our results agree with those obtained by Gutowski et al. (1992). They compared dry and moist baroclinic life cycles and showed that including moisture leads to stronger updrafts as well as to a faster evolution of the life cycle.

Although the temporal and spatial appearance of the TIL is rather heterogeneous in all four simulations, the TIL becomes also evident in the domain mean vertical profiles of N^2. These averages are obtained between $25°$–$65°$ N in the meridional direction and in the entire zonal direction. ΔN^2 represents the difference between the current N^2 and the passively advected tracer N^2_0 (Fig. 6, left panels) and ΔQ the difference between the current potential vorticity Q and the passively advected initial potential vorticity Q_0 (Fig. 6, right panels), respectively. The vertical profiles of ΔN^2 and ΔQ are given in a tropopause based coordinate system for every $24\,\mathrm{h}$ of the model integration and the thin solid line shows the location of the tropopause. In all four simulations an increase in static

stability forms sooner or later during the life cycles just above the tropopause. While the domain mean TIL appears only during the late stages in REF and TURB, it is much earlier obvious in RAD and BMP. However, PV at the tropopause shows significant positive changes only in the simulation with radiation. The location of the maximum diabatic change in PV correlates temporally and spatially (relative to the thermal tropopause) well with the changing gradient of water vapor (see Fig. 4). Moreover, this change in PV occurs over large areas in the model domain (not explicitly shown) and is thus clearly evident in the mean vertical profile of ΔQ. In simulations of real extratropical cyclones over the North Atlantic, the evolution of a dipole structure with a positive PV anomaly above the tropopause and a negative anomaly below have been reported by Chagnon et al. (2013). They could also show that these anomalies are largely related the radiation scheme in their model. In contrast, only minor changes of PV are found in the simulations with turbulence and cloud processes. In the latter case the largest changes of PV occur rather at low- and mid-tropospheric altitudes where the major release of latent heat occurs. These changes occur, however, on smaller spatial areas, and more specifically not always at the same altitude relative to the tropopause. Thus, compared to RAD ΔQ has no pronounced tendency in the domain mean in case of BMP. In the reference case the minor changes of potential vorticity are solely related to the numerics, especially to the tracer advection scheme (Kunkel et al., 2014). Thus, in case of radiation the formation of the TIL is directly related to a diabatic process in the tropopause region, while the diabatic processes related to clouds have an indirect impact on the TIL, i.e., the diabatic processes and the response of the static stability above the tropopause occur at a different places. Mixing, like radiation, also directly affects the TIL but to a much lesser extent.

3.2 Sensitivity of individual diabatic processes

In the next paragraphs we briefly discuss the impact of initial conditions on the model results, focusing especially on experiments with cloud microphysics and radiation.

For microphysics we tested for the amount of initial specific humidity, comparing BMP to BMP R30, and BMP R80, as well as for the representation of the cloud processes, comparing BMP to BMP NOICE, and BMP SATAD. From the temporal evolution of N^2_{max} (Fig. 7a) we infer that the amount of specific humidity is more important than the model formulation of cloud processes. If more water is initially present, then the TIL appears earlier. In contrast, with less initial water the TIL appears later and the entire appearance approximates towards the adiabatic case. Moreover, the occurrence of the TIL is relatively insensitive to the representation of the cloud processes as long as the initial amount of specific humidity is the same as it is the case in BMP, BMP NOICE, and BMP SATAD.

In case of radiation we tested for the initial amount and distribution of water, comparing RAD to RAD R30, and RAD woSW, as well as for the amount of ozone, comparing RAD to RAD rO3. We find only minor differences in the evolution of N^2_{max} for the various sensitivity simulations (Fig. 7b). Reducing the amount of water leads to a reduced radiative feedback and thus to a less strong TIL.

Changing the amount of ozone has, in our case, no significant effect at all, however, with the caveat of the simple representation of ozone in our model. The largest difference is found if we completely remove the water in the stratosphere. This results in an artificially large water vapor gradient between the troposphere and the stratosphere. As we have seen before (Fig. 4), a strong water vapor gradient results in a sharp tropopause. A similar result has been discussed by Fusina and Spichtinger (2010) who studied amongst many other features the response of the static stability to the sharpness of a gradient between saturated and unsaturated air.

4 Relative importance of dynamical and diabatic processes on the TIL formation

Until here we provided new insights of the isolated effect of individual physical processes on the formation of the tropopause inversion layer in baroclinic life cycles. Now we turn our discussion to the relative importance of these processes, and especially whether the dynamical or the radiative forcing is more important for the TIL formation and maintenance. For this purpose we use our second set of baroclinic life cycle experiments where we successively increase the number of processes and as such increase complexity. The simulation with cloud processes (BMP) serves as reference while we first add radiation (BMP RAD) and turbulence (BMP TURB) separately and then combine all three processes (BRT). We further add convection (BRTC) and then also surface fluxes of momentum and heat (BRTCS).

The six life cycles evolve similar, all forming a Θ-streamer and anti-cyclonic wave breaking. Again the temperature distribution at the southern tip of the streamer varies most between the individual life cycles (Fig. 8). Moreover, in some cases a smooth Θ-distribution is evident, e.g., BMP TURB, BRT, or BRTC, while the distribution is more variable and shows more small scale features in other life cycles, especially in BRTCS. In all six cases the static stability above the tropopause is larger in the anti-cyclonic part of the wave than in the cyclonic part (not explicitly shown). After 120 h at least two regions with enhanced values of N^2 are evident. One is further to the north along the cold front ahead of the cyclonic center. The other is more located at the south-western edge of the streamer. As evident from the time series in Figure 9 both maxima are related to the outflow of the warm conveyor belt (WCB). This airstream originates in the lower troposphere in the region ahead of the trough axis (e.g., Carlson, 1998). In the WCB moist air masses rapidly ascend within 1-2 days into the upper troposphere, associated with cloud formation, precipitation, and release of latent heat (e.g., Wernli and Davies, 1997; Madonna et al., 2014). The existence of a relation between WCB and TIL has been proposed by Peevey et al. (2014) who used HIRDLS satellite and ECMWF model data to obtain their results. Moreover, Figure 9 shows that enhanced values of static stability above the tropopause are closely related to the location of strong updrafts and cirrus clouds at the time of the first TIL appearance. The cirrus clouds are identified by the cloud ice content below

the tropopause. Note again that we refer to updrafts here, when an air mass has been lifted by at least $2.5\,\mathrm{km}$ since model start. This change in altitude of an air parcel is calculated from the difference of the current altitude z of this air parcel and its initial altitude z_0, which is carried by a passive tracer. We further denote this difference as Δz which is positive if an air parcel raised and negative if an air parcel descended since model start. The static stability is enhanced almost at all times in the center of the WCB outflow, where the ice cloud branches towards the north-west and south-east. From $102\,\mathrm{h}$ onward a second maximum is evident in the south-eastern branch of the ice cloud which moves further to the south in subsequent hours. This maximum is located more in the region where inertia-gravity waves are generated and influence the thermal structure of the tropopause (Kunkel et al., 2014). This influence is such that the static stability maximum keeps its large values almost entirely constant at subsequent hours of the simulation. In case of BRTCS a larger area exhibits enhanced static stability values above the tropopause which is the result of convective activity as we will see later in more detail.

In the following we aim to answer the question why the TIL appears earlier in some life cycles and how the TIL is maintained after it has been generated. We first compare the time of first appearance of the TIL between the six life cycles. Figure 10a–e shows the first $80\,\mathrm{h}$ of model integration for various variables. The initial increase of N^2_{max} can be divided into three sections which are related to the physical processes considered in the respective life cycle (Fig. 10a). The latest TIL appearance after about $65\,\mathrm{h}$ is found when considering only cloud processes and turbulence. Including radiation to the model simulations shifts the time of appearance ten hours ahead, while the earliest TIL formation starts already after about $35\,\mathrm{h}$ in case of considering convection and surface fluxes. This division into three time sectors correlates well with the proxy for strong updrafts Δz. Figure 10b depicts the maximum Δz in the layer between the thermal tropopause and $500\,\mathrm{m}$ below this level, from which we infer that there is strong temporal coincidence between the first appearance of N^2_{max} and updrafts originating at low levels. The earlier appearance of vertically ascending air masses in case with radiation and convection is related to the these processes, since they foster an earlier emerging of updrafts in the model. This finding supports our results from the previous section that moist dynamics including stronger updrafts than in the dry case has a strong impact on the first appearance of the TIL. These lifted air masses further enhance the local convergence of the vertical wind just above the tropopause as we will see later. Moreover, we find good agreement between the temporal increase of N^2_{max} and two tracers for moisture, specific humidity q_{v} (Fig. 10c) and specific cloud ice content q_{i} (Fig. 10d). Thus, the ascending air masses moisten the upper troposphere below the tropopause which, as shown before, supports the TIL formation by differential radiative cooling. The gradual increase of N^2_{max} in case of BRTCS can further be related to another tracer for updrafts, which is the cloud base mass flux which is available for the two simulations in which the convective cloud parameterization is switched on (Fig. 10e). This quantity serves as proxy for convective activity and starts to increase gradually in the case with surface fluxes early during the simulation. Thus,

these findings further support our suggestion from Sect. 3 that vertical motions are the essential key parameter for the initial TIL appearance in baroclinic life cycles with moist diabatic processes.

We further provide evidence that there is not only a temporal but also a spatial coincidence between updrafts and TIL occurrence. Figure 11 shows zonal cross-sections of N^2 for the six simulations along 45° N after 120 h of model integration. Indications of increased static stability are found in all cases above the lifted air masses which reach the tropopause. Clouds often form in the regions of the updrafts and in the lowermost stratosphere we find regions of convergence of the vertical wind. This convergence results from emerging gravity waves from the updrafts, but is also present in regions of propagating inertia-gravity in the eastern most region of the cross-sections. Gravity waves can alter the TIL temporarily during propagation (Otsuka et al., 2014) and possibly permanently by breaking or wave capture (Kunkel et al., 2014). In addition to the effects of dry dynamics, i.e., distribution of cyclonic and anti-cyclonic flow and breaking of the baroclinic wave (see Erler and Wirth, 2011), the effects from updrafts, small-scale convergence, and radiation, contribute most strongly to the TIL formation. Furthermore, note that low-, and mid-tropospheric diabatic heating causes a negative change in PV above the region of maximum heating, thus enhancing the anti-cyclonic flow in the tropopause region above (e.g., Joos and Wernli, 2012; Wernli and Davies, 1997), which further has a positive feedback on the TIL evolution.

To this point we demonstrated that lifted air masses reaching the tropopause level are initially important to form the TIL. However, this could be a transient effect on the static stability in the stratosphere and as such its contribution could decrease over time with other effects becoming more important. One other potential process might be related to the convergence of the vertical wind $\partial w/\partial z$. If this term becomes negative at or just above the tropopause, the static stability is increased in this region (Wirth, 2004). Convergence can occur on small scales when gravity waves are present or on large scales in anti-cyclonic flow. We introduce here another metric to measure the impact of updrafts and convergent regions on enhanced static stability. For this we calculate the domain mean vertical profile of static stability N^2 as well as the mean vertical profile of static stability in regions with strong updrafts $N^2_{\mathrm{d}z}$, i.e., $\Delta z \geq 2.5\,\mathrm{km}$ below the tropopause, and in regions with strong convergence of the vertical wind $N^2_{\mathrm{w}z}$, i.e., $\partial w/\partial z \leq -5.0\times10^{-5}\,\mathrm{s}^{-1}$. We subtract the domain mean from these values to obtain quantitative measures how strong the TIL is enhanced in the respective regions compared to the TIL in the entire domain. Figure 12 shows the tropopause-based vertical profiles of $N^2_{\mathrm{d}z} - N^2$ (upper panel a) and $N^2_{\mathrm{w}z} - N^2$ (lower panel b) for every 24 h. In $N^2_{\mathrm{d}z} - N^2$ a TIL like vertical profile (i.e., with maximum values just above the tropopause) is evident in all six cases, especially in the first days of the simulations. However, the difference becomes smaller with time, which is partly related to the fact that the TIL becomes more evident in the domain mean N^2. Moreover, the number of grid cells contributing to $N^2_{\mathrm{d}z}$ stagnates at later times, indicating the decreasing number of new updrafts over time, which reach the tropopause (compare the numbers in the top left corners in each panel of Fig. 12). The differences $N^2_{\mathrm{w}z} - N^2$ also become smaller above

the tropopause with time, i.e., the TIL like shape is less evident. However, compared to the relative decreases of the differences $N^2_{\mathrm{d}z} - N^2$, the decreases of $N^2_{\mathrm{w}z} - N^2$ over time are relatively smaller. Moreover, the number of grid cells contributing to $N^2_{\mathrm{w}z}$ becomes significantly larger over time and is in most cases also larger than the number for $N^2_{\mathrm{d}z}$. From this we follow that updrafts might be potentially more important during the initial formation of the TIL. In contrast, the convergence of the vertical wind might become relatively more important in maintaining the TIL during later times of the life cycles.

We already saw that moistening the upper troposphere fosters the evolution of the TIL. Since ice clouds also reach the level of the tropopause, we briefly discuss their potential impact on the thermal structure above the tropopause. We only use cloud processes and radiation in this analysis here and exclude the effects of mixing and convection. We conducted a further simulation in which we turned off the cloud radiative feedback (BMP RAD NOCRF) and compare the results to those from a simulation with feedback (BMP RAD) to assess the impact of ice clouds on TIL in the model. From instantaneous vertical profiles of meteorological and tracer quantities within a region which exhibits a TIL and ice clouds up to the tropopause we infer the following points (Fig. 13): (1) the net heating rate is much more negative in the upper troposphere when the forcing is turned on, with the cooling being strongest just below the thermal tropopause (black solid lines); (2) the temperature profile in the UTLS differs significantly between both cases – while there is a clear minimum in the case with cloud radiative forcing, an almost neutral temperature profile is evident in the first two kilometers above the tropopause in BMP RAD NOCRF (black dashed lines); (3) the upper edge of the ice cloud is located slightly above the tropopause in BMP RAD and slightly below in the other case (blue solid lines); (4) the specific humidity has a local maximum at the top of the ice cloud which is stronger in the case with feedback (blue dashed lines); (5) the static stability is increased in both cases with a slightly higher located and stronger maximum in case with feedback (red solid lines); (6) the height tracer indicates lifted air mass in the troposphere below the maximum of static stability, however, with stronger updrafts in the case with feedback (red dashed lines). From points (1), (2), and (5) we conclude that the tropopause can be sharper due to strong differential cooling in the UTLS, if ice clouds are present. Moreover, from (3), (4), and (6) it follows that the potential to moisten the lower stratosphere is also increased which might in turn enhance the radiative formation process of the TIL. Thus, the results from this sensitivity suggest that there is a larger potential to obtain a stronger TIL when clouds reach up to the level of the tropopause. Moreover, this might be of further interest, since ice clouds, or ice super-saturated regions, have been shown to occur frequently in the lower stratosphere (e.g., Spichtinger et al., 2003; Spang et al., 2015).

So far we mainly focused on radiative and moist effects. In the last paragraph we turn to the effect of mixing and analyze where turbulent mixing occurs at the tropopause and whether this spatially and temporally coincides with the appearance of the TIL. Turbulent mixing contributes to the process of small scale stratosphere-troposphere exchange (STE). It has been speculated in several studies that

TIL and STE are causally related beyond a pure spatial coincidence (e.g., Gettelman and Wang, 2015). Kunz et al. (2009) used airborne measurements and ECMWF analysis data from which they concluded that mixing at the tropopause is a synoptic scale process on rather short time scales which, however, enhances the concentration of radiatively active trace gases in the mixing layer. This then leads to an increase in static stability further downwind of the region of the STE event. Thus, they focused on the long term relation between mixing and N^2. On the other hand we see that values of turbulent kinetic energy (TKE) are often increased in regions where a TIL is present (Fig. 14). These values are smaller than in the boundary layer, but nevertheless increased compared to the background values in the tropopause region at other locations and times in our model simulations. Such exchange events may have only spatial extension of a few tenths of kilometers or even less. Müller et al. (2015) recently reported a comparable event based on airborne in-situ measurements of nitrous oxide, ozone, and ice cloud particles. However, since our model is not capable of resolving this process with sufficient accuracy to conduct a quantitative estimate of STE, we will leave a more detailed analysis open to further studies.

5 The TIL in cyclonic life cycle experiments

So far, the discussion of the results focused on the anti-cyclonic life cycle (LC1, Thorncroft et al., 1993). We will now extend the analysis and show results for five selected cyclonic life cycles (LC2). We obtain this life cycle by adding a cyclonic shear to the background state of the LC1 (see Section 2.1). We briefly compare the results of the LC1 and LC2 and discuss the main difference in the following paragraphs. For this we analyze the results from a dry reference experiment (REF LC2), from three simulations with one additional diabatic process, i.e., with clouds (BMP LC2), with radiation (RAD LC2), and with turbulence (TURB LC2), and from one simulation with a more complex setup including clouds and convection, radiation, and turbulence (BRTC LC2).

Generally, LC2 experiments show a less strong deepening of the minimum surface pressure compared to their LC1 counterparts (Fig. 15a). Similarly to the LC1 waves, the deepening of the surface cyclone is less strong, when radiation is included in the simulations (RAD LC2, BRTC LC2). N^2_{max} above the thermal tropopause shows several differences between LC1 and LC2. In the cases without moisture (REF LC2, RAD LC2, and TURB LC2) the maximum values are always below $7.0 \times 10^{-4}\,\text{s}^{-2}$. Moreover, in contrast to the sudden increase of N^2_{max} in all moist LC1 cases, N^2_{max} increases rather stepwise, in particular in the BMP LC2 case. The absolute maximum is reached only after $110\,\text{h}$ after simulation start and thus much later than in the LC1 BMP case (compare Fig. 3b). Furthermore, at the end of the simulated period N^2_{max} is almost equal in all LC1 cases, which is, however, not the case in the LC2 cases. The TIL area ($A_{5.5}$, see Figure 15c) is largest for BMP LC2 and shows even comparable numbers to its LC1 counterpart. However, in the other cases the $A_{5.5}$ is much smaller in the LC2 cases than in the LC1 cases. Thus, the TIL evolves less strong in amplitude

and spatial extent in the LC2 compared to the LC1. Generally, this is in agreement with the results from Erler and Wirth (2011) for dry adiabatic life cycles.

The processes relevant for the TIL formation are rather similar between LC1 and LC2. In the moist cases BMP LC2 and BRTC LC2 N^2_{max} shows a strong correlation to Δz (see Figure 15d) and thus updrafts may be as important in the LC2 as they are in the LC1 to initially form the TIL in the life cycles. This relation is further obvious when the spatial co-occurrence between lifted air masses and enhanced static stability is studied (Figure 16). The first enhancement of N^2 in the lower stratosphere are again present just above regions which exhibit strong updrafts and also ice clouds just below the tropopause. Thus, except for the difference in the timing of the first vertical ascent patterns, there is no major difference to the LC1 baroclinic life cycle. However, the temporal variability of N^2_{max} in BMP LC2 and BRTC LC2 is slightly larger than in their LC1 counterparts. This might be related to the less strong evolving gravity waves in the LC2 simulations. In particular, gravity waves from the jet-front system are much more evident in LC1 than in LC2 which has been discussed in Kunkel et al. (2014). Thus, the effect of gravity waves on the TIL maintenance might be less strong in case of LC2. Taken together the LC2 cases generally show a less strong developed TIL compared with their LC1 counterparts. Nevertheless, the physical processes leading the TIL formation seem to be similar in LC1 and LC2.

6 Conclusions and summary

By conducting various simulations of baroclinic life cycles we aimed to improve the understanding whether dynamical or diabatic processes are more relevant to form a tropopause inversion layer (TIL). For this we used the non-hydrostatic, limited area model COSMO in a midlatitude channel configuration along with a varying number of physical parameterizations. We first analyzed the effect of individual diabatic processes, i.e., related to clouds, radiation, and mixing processes before we estimated the relative importance of each process.

In a first set of simulations the evolution of the TIL has been compared in baroclinic life cycles. A life cycle experiment with only dry dynamics served as reference case, while three additional life cycle experiments have been performed with individual non-conservative process added. We further assessed the impact of initial conditions and process formulation in the diabatic cases. In a second step we successively increased the number of processes to assess the relative importance of the various dynamical and diabatic processes to the TIL evolution. We further conducted sensitivity experiments to study differences between life cycles of type 1 (LC1) and 2 (LC2).

Most importantly, our experiments highlighted the role of different moisture related processes for the formation and evolution of the TIL with varying relevance and strength in different phases of the baroclinic life cycles. In detail, we derived the following results:

1. A TIL forms in baroclinic life cycles with only dry dynamics as well as in life cycles with additionally either vertical turbulence, cloud processes, or radiation. Compared to the dry reference case the TIL appears weaker with respect to its maximum value as well as to the spatial appearance in the case with turbulence. The opposite is evident in the case with radiation with a larger maximum static stability and larger spatial appearance. The temporal evolution is, however, still similar to the reference case. This is different with cloud processes. The TIL emerges much earlier and shows generally the largest maximum values and spatial extension.

2. The processes forming the TIL in the cases with diabatic processes are as follows. Turbulence acts against the forming process from dynamics, and as such a weaker TIL is the final result. With only radiative processes, the (passive) transport of moisture from low to high levels leads to an increase in the moisture burden in the UTLS and to a change in the moisture gradient in this region. The UTLS is then cooled non-uniformly which finally further enhances the static stability above the tropopause. The important process with clouds is the release of latent heat during condensation. This increases the frequency and strength of vertical motions which locally increase the static stability above the regions of the updrafts. Especially, the TIL forms in the region of the warm conveyor belt. In contrast to the direct diabatic forcing (occurring in the region of the tropopause) in the case with radiation, the enhancement of static stability results from a diabatic forcing at lower levels in the case with clouds.

3. Analysis of initial conditions and process formulations showed that the TIL formation in the model is relatively insensitive to the formulation of the cloud forming process itself and more dependent on the initial amount of specific humidity. For radiation no significant dependency on the initial water or ozone amount is evident. Here, the change of the gradient of specific humidity is the more important process.

4. Further simulations of baroclinic life cycles with varying complexity with respect to the number of incorporated physical processes showed that there is a correlation between the first appearance of the TIL and of updrafts reaching the tropopause. However, the exact timing of this first occurrence further depends on the included physical processes. The TIL emerges latest when only cloud processes and turbulence are considered while it appears earlier when radiation is incorporated and even more with convection. From this result it is concluded that vertically ascending air masses which reach the tropopause altitude are the key process in the initial formation of the TIL in moist baroclinic life cycles, however, noting that their effect is probably fading with time.

5. The updrafts that reach the tropopause lead to the emission of gravity wave in the lower stratosphere. Such small scale waves have a further source in the jet-front system (inertia-gravity waves). In recent studies (e.g., Kunkel et al., 2014; Otsuka et al., 2014) it has been shown that

these small-scale disturbances can alter the thermal structure above the tropopause temporarily as well as permanently and as such affect the TIL during the entire life cycle after their first appearance. At least in parts, the appearance and strength of such gravity waves might explain the weaker appearance of the TIL in the cyclonic life cycles compared to their anti-cyclonic counterparts.

6. Finally, air masses lifted from moist, low-tropospheric regions enhance the moisture content of the upper troposphere, not only by transporting water vapor to this altitude. Clouds also form within the updrafts and locally alter the thermal structure of the upper troposphere. Especially, at the top of the clouds a strong cooling can occur which further contributes to the formation and maintenance of a strong TIL. In general, radiative impacts become more relevant during later stages of the life cycle.

Thus, the various dynamical and diabatic processes lead to a highly variable temporal and spatial appearance of the TIL on the time-scale of a week. While updrafts are important for the first appearance of the TIL when moisture is included in the baroclinic life cycles, the radiative effects as well as the convergence of the vertical wind are more important in maintaining the TIL during later phases of the life cycles. In reality the TIL in the midlatitudes may be restrengthened by each passing baroclinic wave and the lifted water vapor serves as a cooling agent in the upper troposphere and even in the lower stratosphere over a longer time-scale than a week. Taking into account that baroclinic waves occur relatively frequent at midlatitudes, especially from autumn to spring, might further help to explain the quasi-permanent appearance of a layer of enhanced static stability.

Acknowledgements. D. Kunkel acknowledges funding from the German Science Foundation under grant HO 4225/2-1. The authors thank A. Roches, U. Blahak, and S. Schemm for model support and the HPC team of the university of Mainz for computing time. We further thank P. Spichtinger for valuable comments on an earlier version of the manuscript. The comments on the discussion paper from S. Schemm, G. Craig, and an anonymous referee helped to significantly improve the final manuscript. Further information on data (model code and output) relevant to this paper can be obtained upon request via email to the authors (dkunkel@uni-mainz.de).

References

Bell, S. W. and Geller, M. A.: Tropopause inversion layer: seasonal and latitudinal variations and representation in standard radiosonde data and global models, J. Geophys. Res.-Atmos., 113, D05109, doi:10.1029/2007JD009022, 2008.

Birner, T.: Fine-scale structure of the extratropical tropopause region, J. Geophys. Res., 111, D04104, doi:10.1029/2005JD006301, 2006.

Birner, T.: Residual Circulation and Tropopause Structure, J. Atmos. Sci., 67, 2582–2600, doi:10.1175/2010JAS3287.1, 2010.

Birner, T., Dörnbrack, A., and Schumann, U.: How sharp is the tropopause at midlatitudes?, Geophys. Res. Lett., 29, 1700, doi:10.1029/2002GL015142, 2002.

Birner, T., Sankey, D., and Shepherd, T. G.: The tropopause inversion layer in models and analyses, Geophys. Res. Lett., 33, L14804, doi:10.1029/2006GL026549, 2006.

Carlson, T. N.: Mid-Latitude Weather Systems, Amer. Meteor. Soc., 507 pp., 1998.

Chagnon, J. M. Gray, S. L., and Methven, J.: Diabatic processes modifying potential vorticity in a North Atlantic cyclone, Q. J. Roy. Meteor. Soc., 139, 1270–1282, doi:10.1002/qj.2037, 2013.

Doms, G.: A Description of the Nonhydrostatic Regional COSMO-Model, Part I: Dynamics and Numerics, Tech. rep., Deutscher Wetterdienst, Offenbach, Germany, 2011.

Erler, A. R. and Wirth, V.: The static stability of the tropopause region in adiabatic baroclinic life cycle experiments, J. Atmos. Sci., 68, 1178–1193, doi:10.1175/2010JAS3694.1, 2011.

Fusina, F. and Spichtinger, P.: Cirrus clouds triggered by radiation, a multiscale phenomenon, Atmos. Chem. Phys., 10, 5179–5190, doi:10.5194/acp-10-5179-2010, 2010.

Gettelman, A. and Wang, T.: Structural diagnostics of the tropopause inversion layer and its evolution, J. Geophys. Res.-Atmos., 120, 46–62, doi:10.1002/2014JD021846, 2015.

Grise, K. M., Thompson, D. W. J., and Birner, T.: A global survey of static stability in the stratosphere and upper troposphere, J. Climate, 23, 2275–2292, doi:10.1175/2009JCLI3369.1, 2010.

Gutowski, W. J., Branscome, L. E., and Stewart, D. A.: Life cycles of moist baroclinic eddies, J. Atmos. Sci., 49, 306–319, doi:10.1175/1520-0469(1992)049<0306:LCOMBE>2.0.CO;2, 1992.

Held, I. M. and Suarez, M. J.: A proposal for the intercomparison of the dynamical cores of atmospheric general circulation models, B. Am. Meteorol. Soc., 75, 1825–1830, doi:10.1175/1520-0477(1994)075<1825:APFTIO>2.0.CO;2, 1994.

Joos, H. and Wernli, H.: Influence of microphysical processes on the potential vorticity development in a warm conveyor belt: a case-study with the limited-area model COSMO, Q. J. Roy. Meteor. Soc., 138, 407–418, doi:10.1002/qj.934, 2012.

Kunkel, D., Hoor, P., and Wirth, V.: Can inertia-gravity waves persistently alter the tropopause inversion layer?, Geophys. Res. Lett., 41, 7822–7829, doi:10.1002/2014GL061970, 2014.

Kunz, A., Konopka, P., Müller, R., Pan, L. L., Schiller, C., and Rohrer, F.: High static stability in the mixing layer above the extratropical tropopause, J. Geophys. Res., 114, D16305, doi:10.1029/2009JD011840, 2009.

Madonna, E., Wernli, H., Joos, H. and Martius, O.: Warm conveyor belts in the ERA-Interim data set (1979-2010). Part I: Climatology and potential vorticity evolution, J. Climate, 27, 3-26, 2014

Mellor, G. L. and Yamada, T.: Development of a turbulence closure model for geophysical fluid problems, Rev. Geophys., 20, 851, doi:10.1029/RG020i004p00851, 1982.

Müller, S., Hoor, P., Berkes, F., Bozem, H., Klingebiel, M., Reutter, P., Smit, H. G. J., Wendisch, M., Spichtinger, P., and Borrmann, S.: In situ detection of stratosphere-troposphere exchange of cirrus particles in the midlatitudes, Geophys. Res. Lett., 42, 949–955, doi:10.1002/2014GL062556, 2015.

Murray, F. W.: On the computation of saturation vapor pressure, J. Appl. Meteorol., 6, 203–204, doi:10.1175/1520-0450(1967)006<0203:OTCOSV>2.0.CO;2, 1967.

Olson, J. B. and Colle, B.: A modified approach to initialize an idealized extratropical cyclone within a mesoscale model, Mon. Weather Rev., 135, 1614–1624, doi:10.1175/MWR3364.1, 2007.

Otsuka, S., Takeshita, M., and Yoden, S.: A numerical experiment on the formation of the tropopause inversion layer associated with an explosive cyclogenesis: possible role of gravity waves, Progress in Earth and Planetary Science, 1, 19, doi:10.1186/s40645-014-0019-0, 2014.

Peevey, T. R., Gille, J. C., Homeyer, C. R., and Manney, G. L.: The double tropopause and its dynamical relationship to the tropopause inversion layer in storm track regions, J. Geophys. Res.-Atmos., 119, 10194–10212, doi:10.1002/2014JD021808, 2014.

Randel, W. J. and Wu, F.: The Polar summer tropopause inversion layer, J. Atmos. Sci., 67, 2572–2581, doi:10.1175/2010JAS3430.1, 2010.

Randel, W. J., Wu, F., and Forster, P.: The extratropical tropopause inversion layer: global observations with GPS data, and a radiative forcing mechanism, J. Atmos. Sci., 64, 4489–4496, doi:10.1175/2007JAS2412.1, 2007.

Riese, M., Ploeger, F., Rap, A., Vogel, B., Konopka, P., Dameris, M., and Forster, P.: Impact of uncertainties in atmospheric mixing on simulated UTLS composition and related radiative effects, J. Geophys. Res., 117, D16305, doi:10.1029/2012JD017751, 2012.

Ritter, B. and Geleyn, J.-F.: A comprehensive radiation scheme for numerical weather prediction models with potential applications in climate simulations, Mon. Weather Rev., 120, 303–325, doi:10.1175/1520-0493(1992)120<0303:ACRSFN>2.0.CO;2, 1992.

Schemm, S., Wernli, H., and Papritz, L.: Warm conveyor belts in idealized moist baroclinic wave simulations, J. Atmos. Sci., 70, 627–652, doi:10.1175/JAS-D-12-0147.1, 2013.

Son, S.-W. and Polvani, L. M.: Dynamical formation of an extra-tropical tropopause inversion layer in a relatively simple general circulation model, Geophys. Res. Lett., 34, L17806, doi:10.1029/2007GL030564, 2007.

Spang, R., Günther, G., Riese, M., Hoffmann, L., Müller, R., and Griessbach, S.: Satellite observations of cirrus clouds in the Northern Hemisphere lowermost stratosphere, Atmos. Chem. Phys., 15, 927–950, doi:10.5194/acp-15-927-2015, 2015.

Spichtinger, P., Gierens, K., Leiterer, U., and Dier, H.: Ice supersaturation in the tropopause region over Lindenberg, Germany, Meteorol. Z., 12, 143–156, doi:10.1127/0941-2948/2003/0012-0143, 2003.

Sprenger, M., Croci Maspoli, M., and Wernli, H.: Tropopause folds and cross-tropopause exchange: a global investigation based upon ECMWF analyses for the time period March 2000 to February 2001, J. Geophys. Res.-Atmos., 108, 8518, doi:10.1029/2002JD002587, 2003.

Table 1. Summary of experiment acronyms, description, and water treatment

Experiment	Short description	Water species
REF	adiabatic reference simulation	no water species
BMP	standard cloud microphysics	interactive water
RAD	standard radiation scheme	passive water vapor
TURB	standard turbulence scheme	no water species
BMP R30	BMP sensitivity, reduced specific water vapor	interactive water
BMP R80	BMP sensitivity, increased specific water	interactive water
BMP NOICE	BMP sensitivity, only warm clouds	interactive water, no ice phase
BMP SATAD	BMP sensitivity, saturation adjustment	water vapor and cloud water
RAD woSW	RAD sensitivity, no stratospheric water	passive water vapor
RAD R30	RAD sensitivity, reduced specific water vapor	passive water vapor
RAD rO3	RAD sensitivity, reduced ozone concentration	passive water vapor
BMP RAD	cloud microphysics and radiation	interactive water
BMP RAD NOCRF	cloud microphysics and radiation no cloud radiative feedback	interactive water
BMP TURB	cloud microphysics and turbulence	interactive water
BRT	cloud microphysics, radiation, and turbulence	interactive water
BRTC	cloud microphysics, radiation, turbulence, and convection	interactive water
BRTCS	cloud microphysics, radiation, turbulence, convection, and surface fluxes for momentum and heat	interactive water
REF LC2	adiabatic reference simulation for LC2	no water species
BMP LC2	standard cloud microphysics for LC2	interactive water
RAD LC2	standard radiation scheme for LC2	passive water vapor
TURB LC2	standard turbulence scheme for LC2	no water species
BRTC LC2	cloud microphysics, radiation, turbulence, and convection for LC2	interactive water

Steppeler, J., Doms, G., Schättler, U., Bitzer, H. W., Gassmann, A., Damrath, U., and Gregoric, G.: Meso-gamma scale forecasts using the nonhydrostatic model LM, Meteorol. Atmos. Phys., 82, 75–96, doi:10.1007/s00703-001-0592-9, 2003.

Thorncroft, C. D., Hoskins, B. J., and McIntyre, M. E.: Two paradigms of baroclinic-wave life-cycle behaviour, Q. J. Roy. Meteor. Soc., 119, 17–55, doi:10.1002/qj.49711950903, 1993.

Tiedtke, M.: A comprehensive mass flux scheme for cumulus parameterization in large-scale models, Mon. Weather Rev., 117, 1779–1800, doi:10.1175/1520-0493(1989)117<1779:ACMFSF>2.0.CO;2, 1989.

Wernli, H. and Davies, H. C.: A Lagrangian-based analysis of extratropical cyclones. I: The method and some applications, Q. J. Roy. Meteor. Soc., 123, 467–489, doi:10.1002/qj.49712353811, 1997.

Wirth, V.: Static stability in the extratropical tropopause region, J. Atmos. Sci., 60, 1395–1409, doi:10.1175/1520-0469(2003)060<1395:SSITET>2.0.CO;2, 2003.

Wirth, V.: A dynamical mechanism for tropopause sharpening, Meteorol. Z., 13, 477–484, 2004.

WMO (1957), Meteorology - a three dimensional science, *WMO Bulletin*, pp. 134–138.

Zierl, B. and Wirth, V.: The influence of radiation on tropopause behavior and stratosphere-troposphere exchange in an upper tropospheric anticyclone, J. Geophys. Res., 102, 23883, doi:10.1029/97JD01667, 1997.

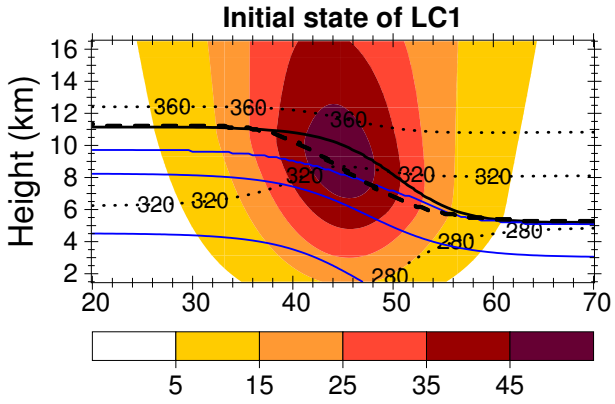

Figure 1. Meridional cross section of the initial state at the center of the model domain: the zonal wind U is color-coded for values of 5, 15, 25, 35, and 45 ms^{-1}; the potential temperature Θ is shown by the black dotted lines for 280, 320, and 360 K (from bottom to top); the water vapor mixing ratio is shown by the blue lines for values of 2.0, 0.2, and $0.02\,\mathrm{gkg}^{-1}$ (from bottom to top); the location of thermal tropopause is indicated by the solid thick black line and separates also the region of tropospheric values ($N^2 < 1.5 \times 10^{-4}\,\mathrm{s}^{-2}$) from stratospheric values ($N^2 \sim 4.0 \times 10^{-4}\,\mathrm{s}^{-2}$) of static stability; the location of the dynamical tropopause, defined as the isosurface of potential vorticity $Q = 2.0\,\mathrm{pvu}$, is shown by the dashed thick line.

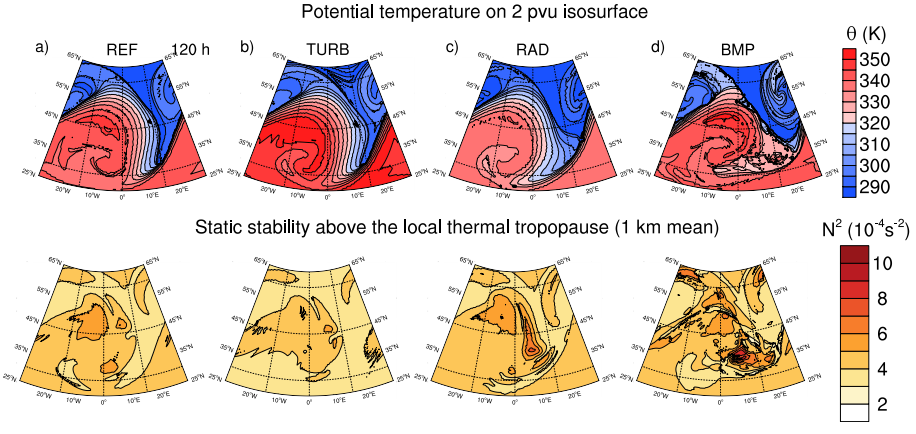

Figure 2. Dynamical and thermodynamical state of the baroclinic life cycles after 120 h of model integration. In the upper row the distribution of potential temperature Θ (in K) on the dynamical tropopause is depicted, while the lower row shows the distribution of static stability N^2 (in $10^{-4}\,\mathrm{s}^{-2}$) averaged over the first kilometer above the thermal tropopause. The four columns show from left to right the following simulations: **(a)** REF, **(b)** TURB, **(c)** RAD, and **(d)** BMP.

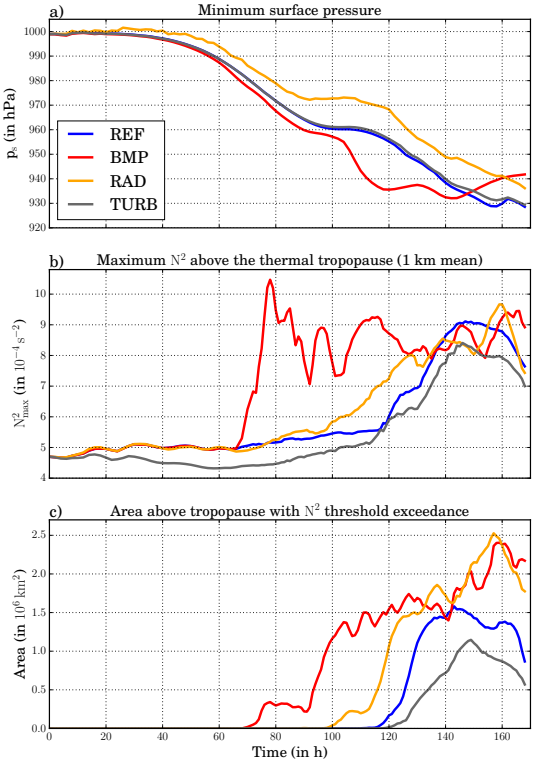

Figure 3. Temporal evolution over the entire simulated life cycles of **(a)** the minimum surface pressure p_s (in hPa), **(b)** the maximum static stability N^2_max (in $10^{-4}\,\mathrm{s}^{-2}$) above the thermal tropopause, and **(c)** the area $A_{5.5}$ (in $10^6\,\mathrm{km}^2$) of N^2 threshold exceedance above the thermal tropopause (with a threshold of $N^2 = 5.5 \times 10^{-4}\,\mathrm{s}^{-2}$). The colored lines indicate the following simulations: REF (blue), BMP (red), RAD (orange), and TURB (gray).

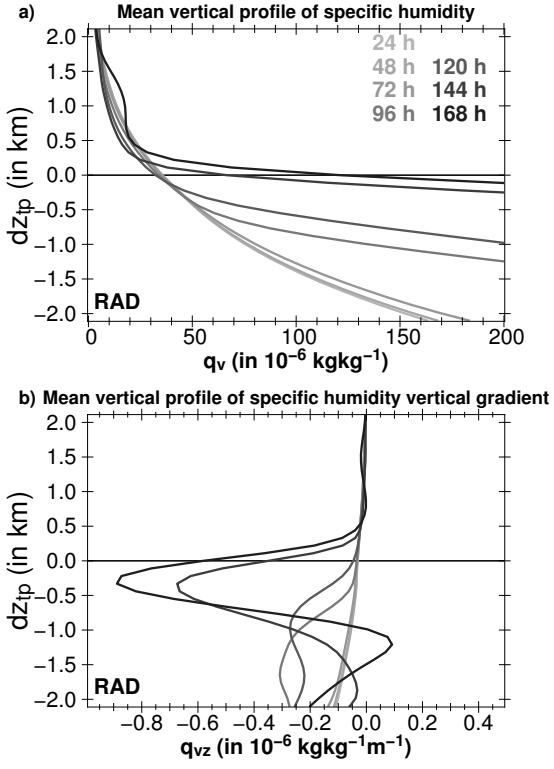

Figure 4. Instantaneous thermal tropopause based domain mean values of **(a)** specific humidity q_{v} (in $10^{-6}\,\mathrm{kg\,kg^{-1}}$) and **(b)** the vertical gradient of specific humidity $\partial q_{\mathrm{v}}/\partial z$ (in $10^{-6}\,\mathrm{kg\,kg^{-1}\,m^{-1}}$) for RAD. The domain mean is calculated within 25–65° latitude and the entire zonal domain. dz_{tp} is the distance to the height of the thermal tropopause. The intensity of the gray colors indicates the time since model start in 24 h intervals.

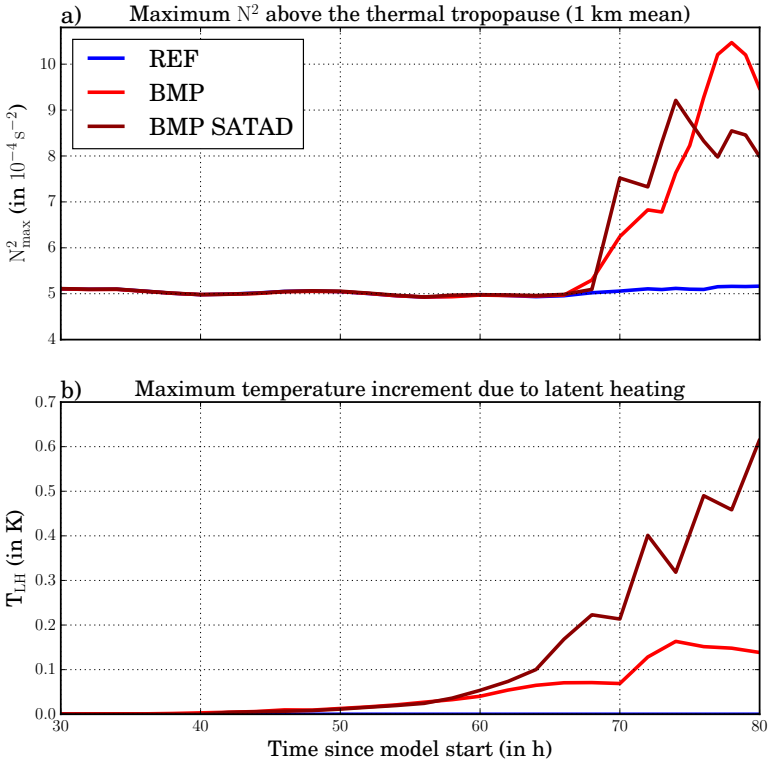

Figure 5. Temporal evolution between 30 h and 80 h after simulation start of **(a)** the maximum static stability N^2_{max} (in $10^{-4}\,\text{s}^{-2}$) above the thermal tropopause and **(b)** the maximum temperature increment due to latent heating T_{LH} (in K) in the model domain for REF (blue lines), BMP (red lines), and BMP SATAD (dark red lines).

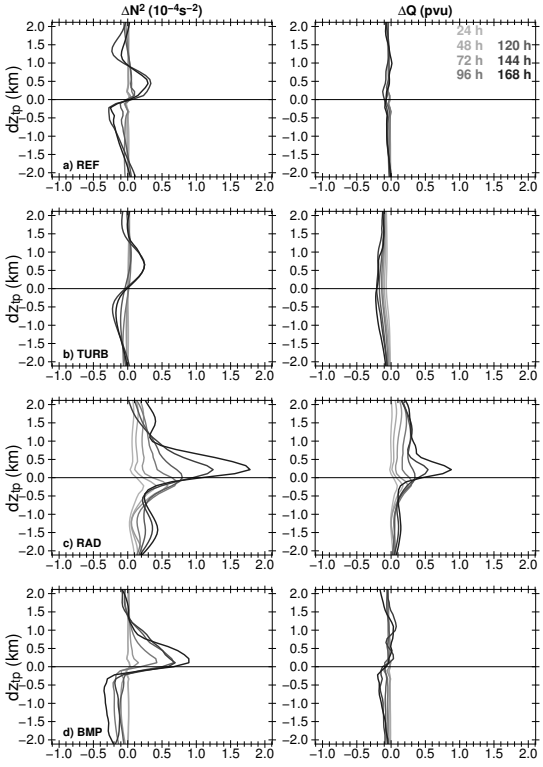

Figure 6. Instantaneous thermal tropopause based domain mean values of ΔN^2 (in $10^{-4}\,\mathrm{s}^{-2}$) in the left panels and ΔQ (in pvu) in the right panels for **(a)** REF, **(b)** TURB, **(c)** RAD, and **(d)** BMP. The domain mean is calculated within 25–65° latitude and the entire zonal domain. The intensity of the gray colors indicates the time since model start in 24 h intervals. ΔN^2 is the difference between the current static stability N^2 and the advected initial static stability N_0^2, ΔQ is the difference between the current potential vorticity Q and the advected initial potential vorticity Q_0. dz_{tp} is the distance to the height of the thermal tropopause.

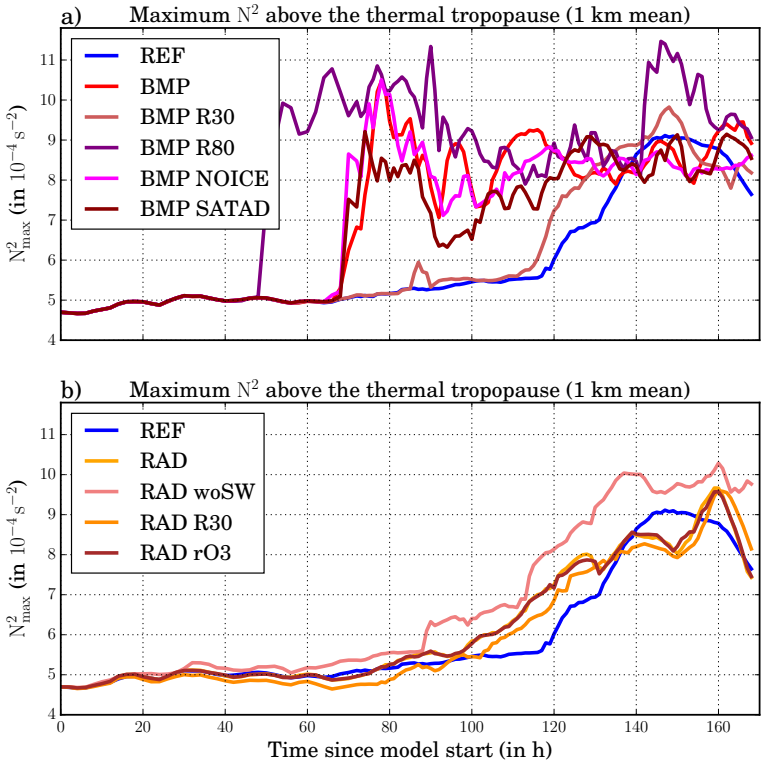

Figure 7. Temporal evolution of the maximum static stability N^2_{max} (in $10^{-4}\,\mathrm{s}^{-2}$) above the thermal tropopause for sensitivity simulations of **(a)** BMP and **(b)** RAD. In **(a)** N^2_{max} is shown for REF (blue), BMP (red), BMP R30 (light red), BMP R80 (purple), BMP NOICE (magenta), and BMP SATAD (dark red). In **(b)** N^2_{max} is shown for REF (blue), RAD (orange), RAD woSW (coral), RAD R30 (dark orange), and RAD rO3 (brown).

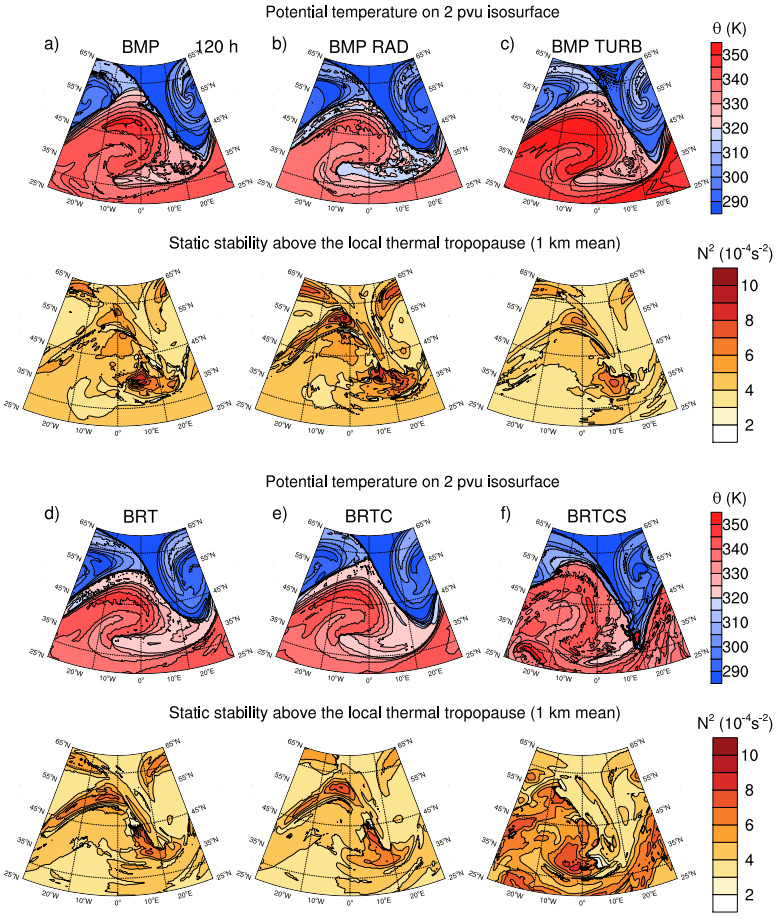

Figure 8. Dynamical and thermodynamical state of baroclinic life cycles after 120 h of model integration. In the upper rows of the six panels the distribution of potential temperature Θ (in K) on the dynamical tropopause is depicted, while the lower rows show the distribution of static stability N^2 (in $10^{-4}\,\mathrm{s}^{-2}$) averaged over the first kilometer above the thermal tropopause for **(a)** BMP, **(b)** BMP RAD, **(c)** BMP TURB, **(d)** BRT, **(e)** BRTC, and **(f)** BRTCS.

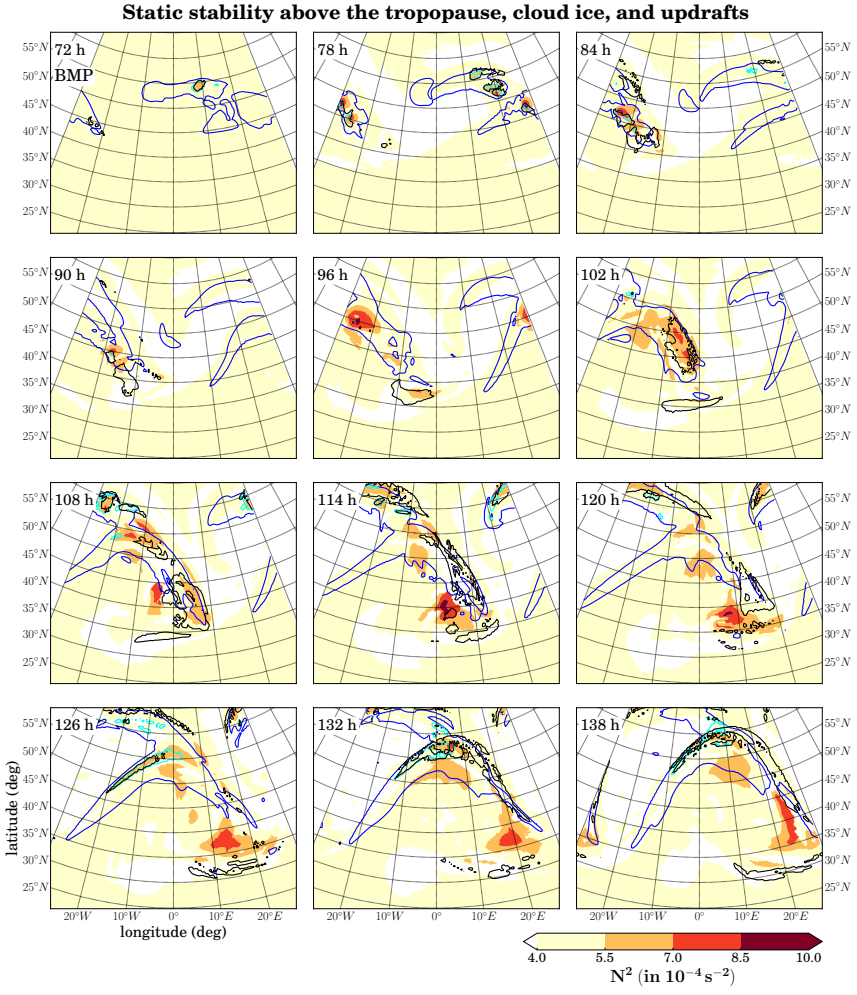

Figure 9. Static stability N^2 (color-coded, in $10^{-4}\,\mathrm{s}^{-2}$) above the thermal tropopause, Δz (black lines, in $2.5\,\mathrm{km}$), column integrated cloud ice content tq_i (blue lines, in $0.01\,\mathrm{kg\,m}^{-2}$), and tropopause close column integrated cloud ice content $tq_\mathrm{i,tp}$ (cyan lines, in $0.001\,\mathrm{kg\,m}^{-2}$). Tropopause close means the region between the thermal tropopause and $500\,\mathrm{m}$ below. The distribution is shown for BMP between $78\,\mathrm{h}$ and $138\,\mathrm{h}$ after simulation start in a six hourly interval.

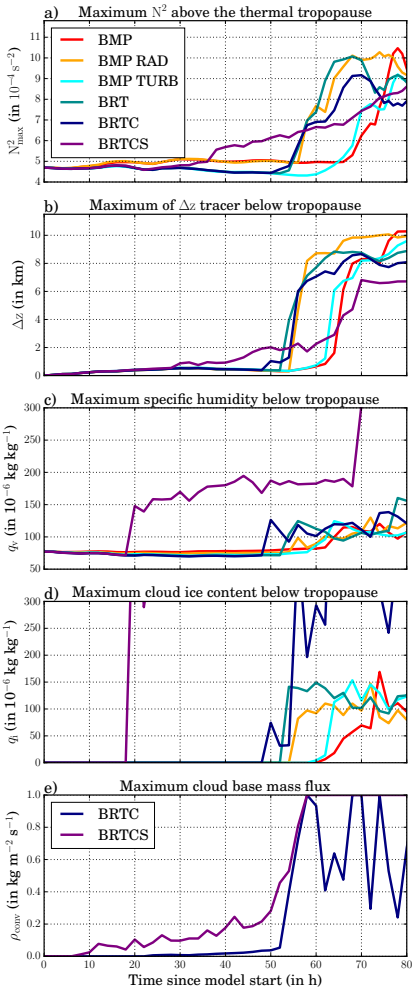

Figure 10. Temporal evolution over the first 80 h of the life cycles of **(a)** N^2_{max} (in $10^{-4}\,\mathrm{s}^{-2}$) above the thermal tropopause, **(b)** the maximum of the Δz tracer (in km) in a 500 m thick layer below the thermal tropopause, **(c)** the maximum specific humidity q_{v} in a 500 m thick layer below the thermal tropopause (in $10^{-6}\,\mathrm{kg\,kg}^{-1}$), **(d)** the maximum specific cloud ice content q_{i} in a 500 m thick layer below the thermal tropopause (in $10^{-6}\,\mathrm{kg\,kg}^{-1}$), and **(e)** the maximum cloud base mass-flux ρ_{CONV} (in $\mathrm{kg\,m}^{-2}\mathrm{s}^{-1}$). The time of TIL occurrence is split into three time sectors. Without radiation and convection, the TIL appears after 65 h, with radiation between 50 h-65 h, and with strong convection before 50 h (more information is given in the text). The colored lines indicate the following simulations: BMP (red), BMP RAD (orange), BMP TURB (cyan), BRT (dark cyan), BRTC (dark blue), and BRTCS (purple).

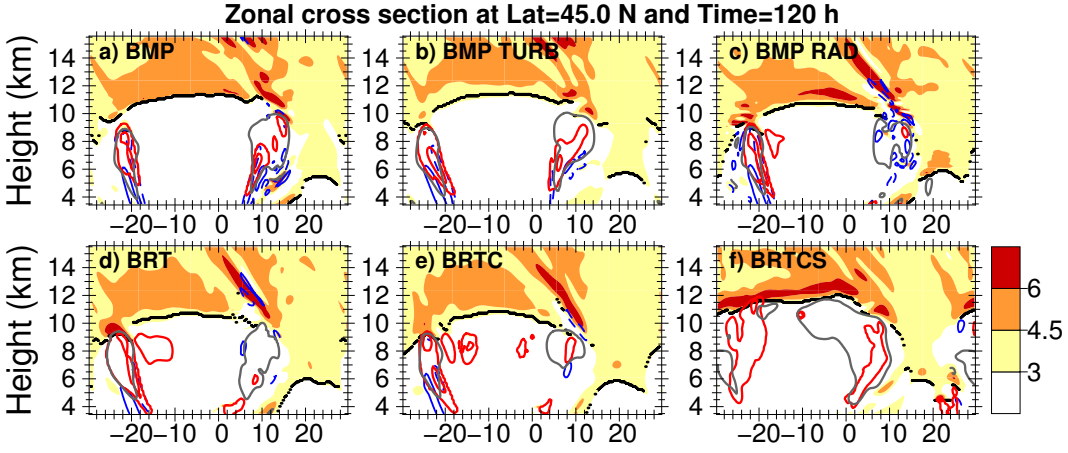

Figure 11. Zonal cross sections along 45° N of static stability N^2 (in $10^{-4}\,\mathrm{s}^{-2}$) after 120 h of model integration. Red lines show specific cloud ice content q_i (for $5.0\times10^{-6}\,\mathrm{kg\,kg}^{-1}$), solid blue lines show regions with positive values of $\partial w/\partial z$ (for $10.0\times10^{-5}\,\mathrm{s}^{-1}$), dashed blue lines show negative values (for $-10.0\times10^{-5}\,\mathrm{s}^{-1}$), and solid gray lines show regions with Δz tracer larger than $2.5\,\mathrm{km}$. The thick black line is the thermal tropopause. The six panels show **(a)** BMP, **(b)** BMP RAD, **(c)** BMP TURB, **(d)** BRT, **(e)** BRTC, and **(f)** BRTCS.

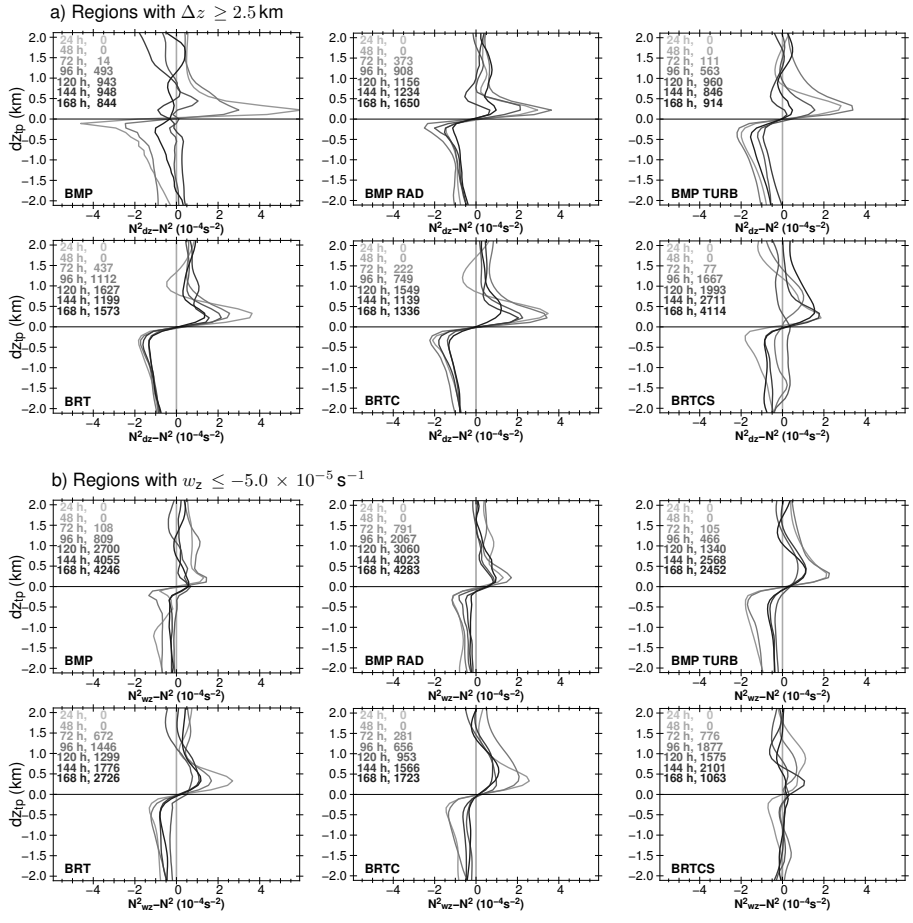

Figure 12. (a) Instantaneous thermal tropopause based vertical profiles of difference between the mean of static stability in regions with $\Delta z > 2.5\,\mathrm{km}$ N^2_{dz} and the domain mean N^2 (in $10^{-4}\,\mathrm{s}^{-2}$) for each 24 h of the model integration. **(b)** Differences for regions with $\partial w/\partial z \leq -5.0 \times 10^{-5}\,\mathrm{s}^{-1}$. The values in the top left corner of each panel show the number of individual profiles used for calculating the respective mean profile of N^2_{dz} and N^2_{wz}. dz_{tp} is the distance to the height of the thermal tropopause.

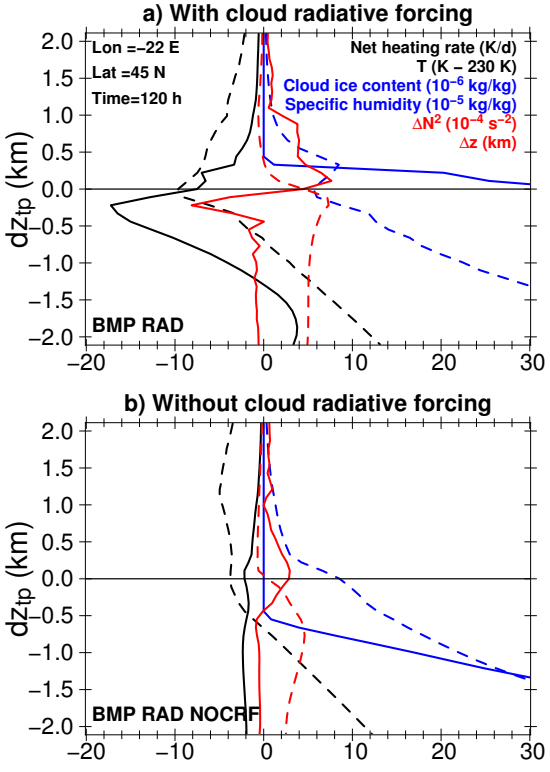

Figure 13. Tropopause based vertical profiles through an ice cloud along the central latitude at 120 h for **(a)** a simulation with cloud radiative forcing (BMP RAD) and **(b)** a simulation without cloud radiative forcing (BMP RAD NOCRF). Solid lines show net radiative heating (in $\mathrm{K\,d^{-1}}$, scaled for better comparability, black), cloud ice content (in $10^{-6}\,\mathrm{kg\,kg^{-1}}$, blue), and ΔN^2 (in $10^{-4}\,\mathrm{s^{-2}}$, red). Dashed lines show temperature (in $\mathrm{K} - 230\,\mathrm{K}$, black), specific humidity (in $10^{-5}\,\mathrm{kg\,kg^{-1}}$, blue), and Δz (in km, red). dz_{tp} is the distance to the height of the thermal tropopause.

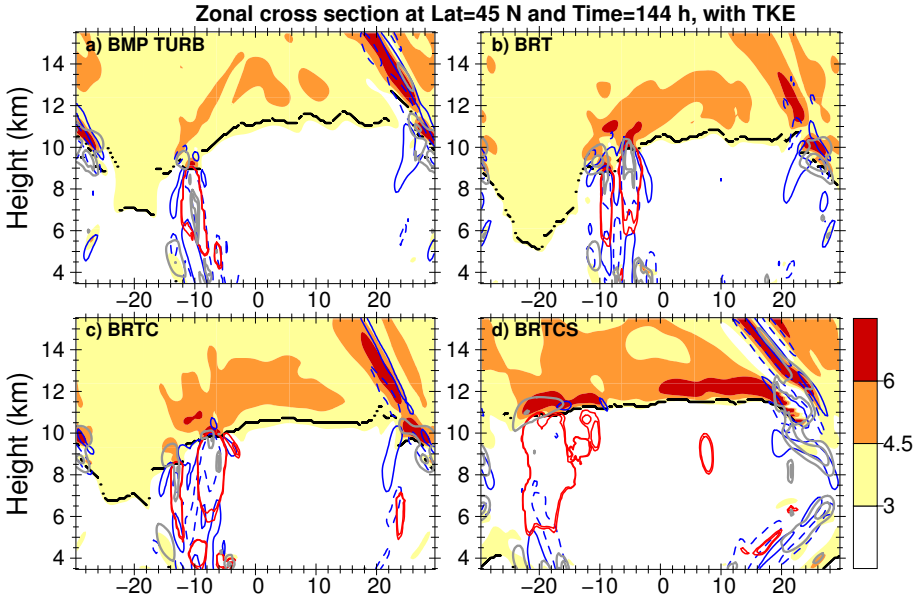

Figure 14. Zonal cross sections along 45° N of static stability N^2 (in $10^{-4}\,\mathrm{s}^{-2}$) after 144 h of model integration. Solid blue lines show regions with positive values of the vertical divergence $\partial w/\partial z$ (for $5.0,\ 50.0 \times 10^{-5}\,\mathrm{s}^{-1}$), dashed blue lines show negative values (for $-5.0,\ -50.0 \times 10^{-5}\,\mathrm{s}^{-1}$). Red lines show specific cloud ice content q_i (for $5.0,\ 10.0,\ \times 10^{-6}\,\mathrm{kg\,kg}^{-1}$). Gray lines show turbulent kinetic energy (TKE) (in $0.5, 1.0, 5.0\,\mathrm{m}^2\mathrm{s}^{-2}$). The four panels show **(a)** BMP TURB, **(b)** BRT, **(c)** BRTC, and **(d)** BRTCS.

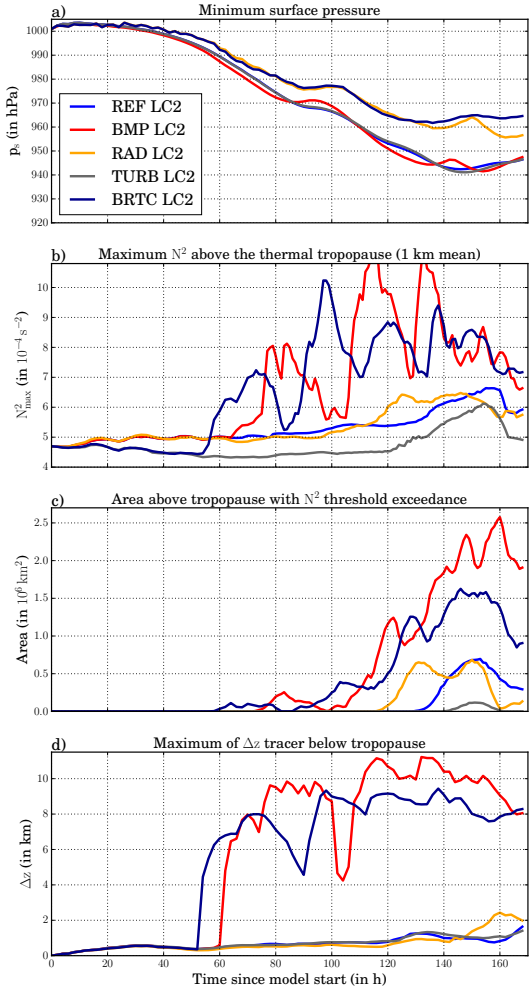

Figure 15. Temporal evolution over the entire simulated life cycles of **(a)** the minimum surface pressure p_s (in hPa), **(b)** the maximum static stability N^2_max (in $10^{-4}\,\mathrm{s}^{-2}$) above the thermal tropopause, **(c)** the area $A_{5.5}$ (in $10^6\,\mathrm{km}^2$) of N^2 threshold exceedance above the thermal tropopause (with a threshold of $N^2 = 5.5 \times 10^{-4}\,\mathrm{s}^{-2}$), and **(d)** the maximum of the Δz tracer (in km) in a 500 m thick layer below the thermal tropopause. The colored lines indicate the following simulations: REF LC2 (blue), BMP LC2 (red), RAD LC2 (orange), TURB LC2 (gray), and BRTC LC2 (dark blue).

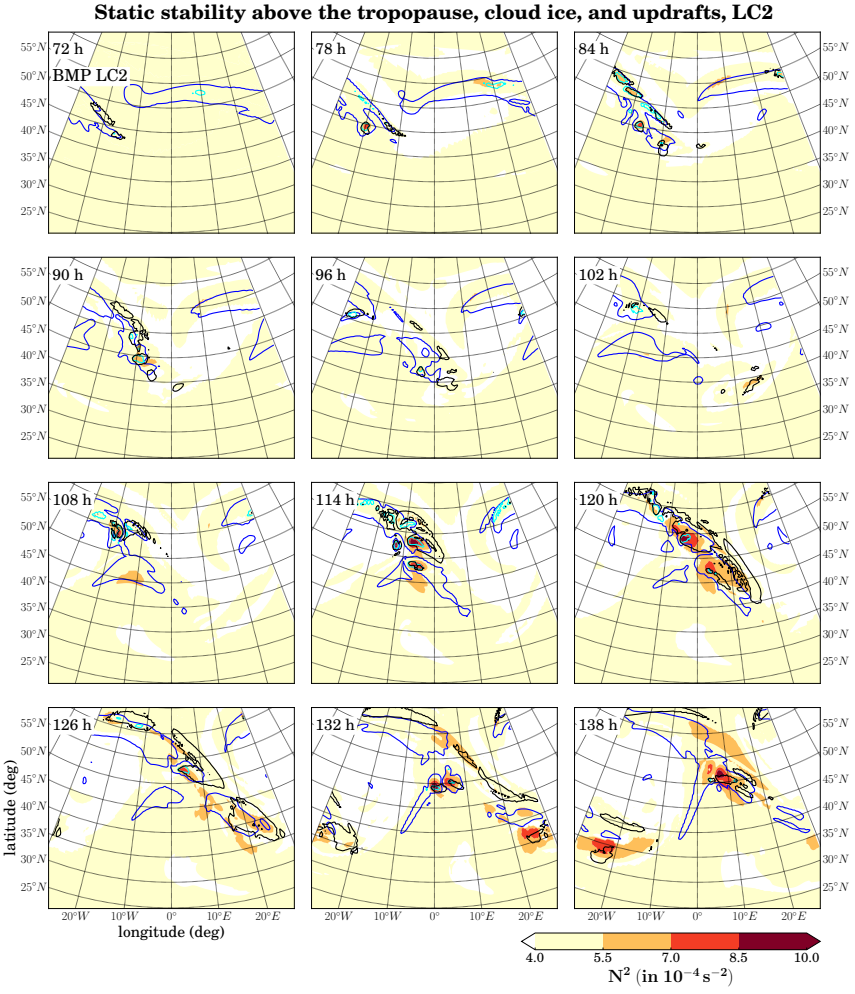

Figure 16. As Figure 9, but for BMP LC2.